Synthetic neutrino imaging of a microquasar

Theodoros Smponias[1]

Directorate of Secondary Education of the Dodekanese, Rhodes, Greece

Abstract

Particle emission from simulated twin microquasar jets is calculated in a unified manner. A program suite assembled around model data produces synthetic images and spectra, directly comparable to potential observations by contemporary arrays. The model is capable of describing a multitude of system geometries, incorporating increasing levels of realism, depending on the needs and on available computational resources. As an application, the modelling process is applied to a typical microquasar, which is synthetically observed from five different angles and with different imaging geometries.

Keywords:

ISM: jets and outflows, stars: winds-outflows, stars: flare, radiation

mechanisms: general, methods: numerical

2010 MSC: 85-08

1. Introduction

Microquasars (MQ) comprise a binary stellar system where a main sequence star orbits a compact object, either a neutron star or a black hole [1]. Matter from the star accretes onto the collapsed stellar remnant, resulting to the production of twin relativistic jets, pointing in opposite directions. Those jets emit over a broad spectrum, from radio to very high energy (VHE) γ-rays and neutrinos [2], [3], [4], [5], [6]).

---

*Corresponding author
Email address:* t.smponias@hushmail.com (Theodoros Smponias)

As mentioned in [2], apparent superluminal motion in certain MQ indicate the presence of bulk hadron flows in the jets. The assumption of equipartition [5], leads to high magnetic field estimates for the jet [7]. This, coupled with the fluid approximation for the jet matter, due to the presence of tangled magnetic fields [8] [9], allows the magneto-hydrodynamic (MHD) approximation for the jets. A toroidal magnetic field component may retain jet collimation over considerable distances along its path [7] [10].

In this paper, the production of very high energy (VHE) neutrinos from generic MQ jets is modelled, using the method of dynamic and radiative relativistic MHD simulation. The paper is organized as follows:

In Section 2 the theoretical background of the work is presented. In Section 3 is obtained the emission of particles from the jet. In Section 4 the results are presented and discussed. The normalization/equipartition (and the synthetic imaging process) are described in the Appendix.

2. Theoretical setup

In our generic MQ model, an accretion disk is assumed around the compact object [11]. Twin jets emanate from the vicinity of the collapsed star, collimated by a toroidal magnetic field component. Adopting a heavier pair of jets, their kinetic power is set to $L_k = 2 \times 10^{38}$ (see Appendix). [5] argue a 10 percent Eddington luminocity jet power, leading to $L_k = 10^{38}$ ergs^{-1} for a 10 M$_\odot$ black hole, which is comparable to our simulation. Furthermore, the same authors argue either $\frac{L_p}{L_e} \simeq 100$ or $\simeq 1$, and in our case we shall adopt the former hypothesis, favouring protons. Equipartition means $\rho_k = \rho_B$, therefore $B(z) = \sqrt{8\pi\rho_z}$ [8] [9], a close match with the B used in the simulation (see Appendix).

2.1. Non-thermal proton density

Neutrino emission from the jets is taken to originate from proton-proton interaction between a distribution of hot (fast) protons and cold (bulk flow) protons [2, 4, 5, 6, 12, 13]. Some of the bulk protons get accelerated at shock

2

fronts, according to the first order Fermi acceleration mechanism, with a time scale of [14], [8], [9]

$$t_{acc}^{-1} \simeq \eta \frac{ceB}{E_p}, \tag{1}$$

where B is the magnetic field and E_p the proton energy, e being the proton charge and c the speed of light. $\eta = 0.1$ represents an acceleration efficiency parameter, assuming efficient acceleration in moderately relativistic shocks in the vicinity of the jet base [14].

In the present work, we adopt a power-law distribution, for the fast protons, of the form $N_p = N_0 E^{-\alpha}$ [15], with either $\alpha \approx 2$ [4], or a variable α [6], where α is the proton spectral index in the local jet cell matter frame. Alternatively, a transport equation could be used to find the distribution [4].

As a further approximation, the aforementioned hot proton distribution is taken to be isotropic in the jet frame, assuming the scattering length l_{sc} is less than the radiative length, l_r, a hypothesis backed by the nature of diffuse shock acceleration [16].

2.2. A note on jet frame anisotropy

For protons accelerated at diffuse scocks, the above assumption of isotropy goes by definition, since at shocks it has to preserve, after every bounce, at least some E, therefore l_{sc} is clearly less than l_r, else it would not have any E left after the bounce!

According to [16], an assumed anisotropy of the hot proton distribution can be reflected to the neutrino distribution. In the jet system, emission would then be projected off axis, even reinforced, under certain orientations, in the lab frame.

3. Neutrino emission calculations

3.1. Proton energy loss

Following [12], [5], and [6], certain energy loss mechanisms are included. This presentation is performed at a cell with the properties
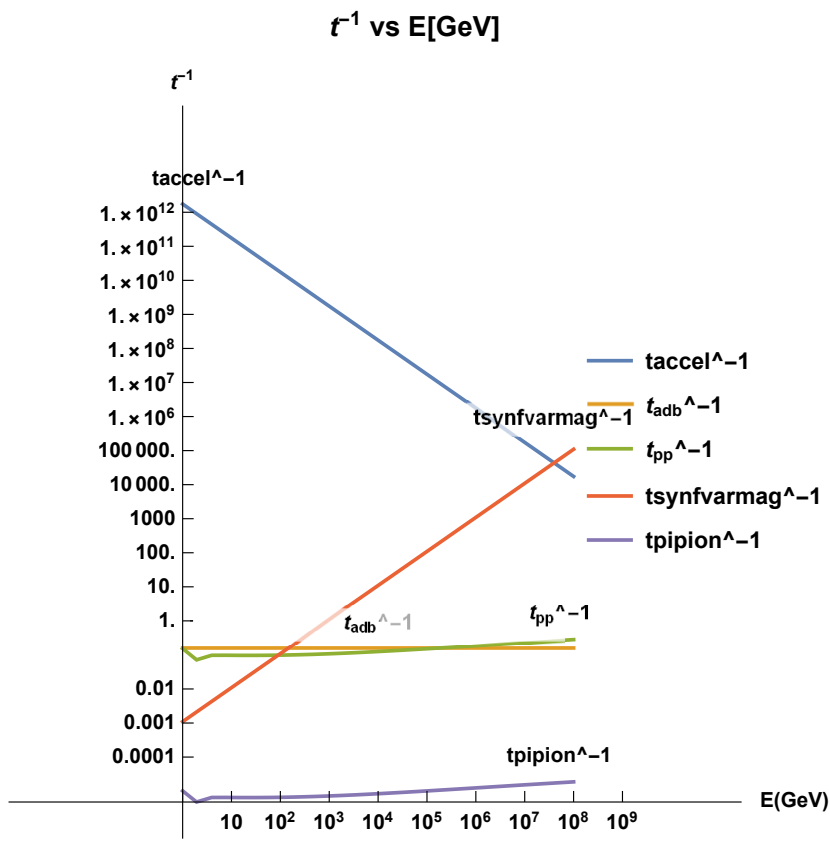
3

Figure 1: High energy proton distribution loss time scales, for various processes in the jets, plotted with energy in erg. t_{pipion} stands for the pion decay timescale t_π.

of:$(u_x, u_y, u_z, b_x, b_y, b_z, n_p, \phi_1, \phi_2, \alpha)$=(-0.3780c, 0.4480c, 0.0124c, 10^5G, 10^6G, 10^5G, 2.1×10^{11}cm^{-3}, 1.047 rad, 5.00$\times$ 10^{-7}rad, 2.0). Nevertheless, in the model runs these are potentially performed in every cell.

We consider a cutoff maximum E for protons of E_{max}=10^6 GeV. For the adiabatic expansion time scale we have [5]

$$t_{adb}^{-1} = \frac{2}{3} \frac{u_{b(adb)}}{z_j} \tag{2}$$

where z_j=10^{11} cm is the characteristic lateral size scale of the jet. For this simple calculation, $u_{b(adb)}$ is preset to 0.8. For the p-p collision loss mechanism, we have

$$t_{pp}^{-1} = nc\sigma_{inel_{pp}}(E_p)K_{pp} \tag{3}$$

$$\sigma_{pp}^{(inel)} = (34.3 + 1.88L + 0.25L^2) \times [1 - (\frac{E_{th}}{E_p})^4]^2 \times 10^{-27} cm^2 \tag{4}$$

σ_{pp}^{inel} is the inelastic p-p scattering cross section.

For the pion decay time we have

$$t_{\pi 0} = 2.6 \times 10^{-8} s \tag{5}$$

4

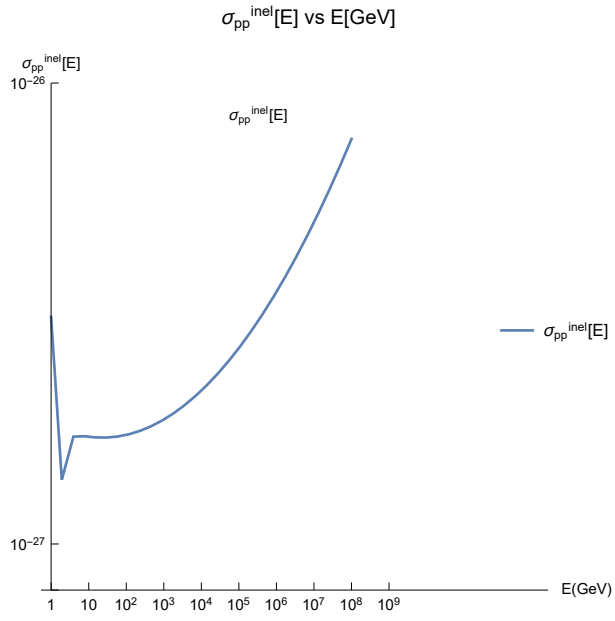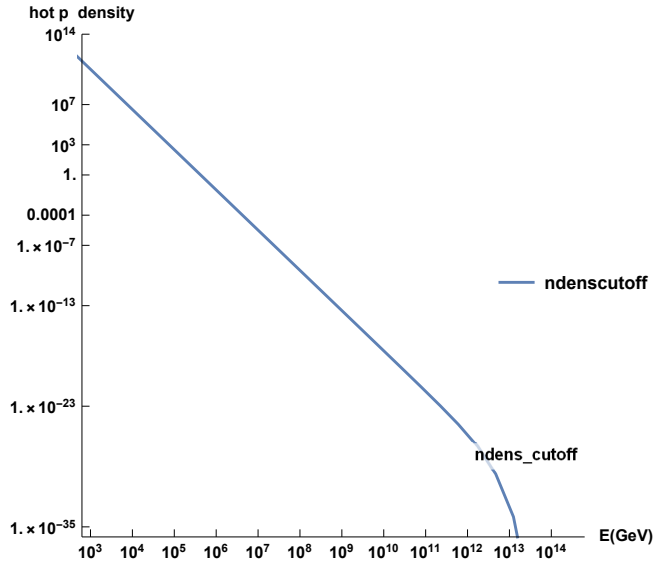Figure 2: Inelastic proton-proton collission standard plotted with energy.

Figure 3: The density of non-thermal protons in the jet is plotted with energy.
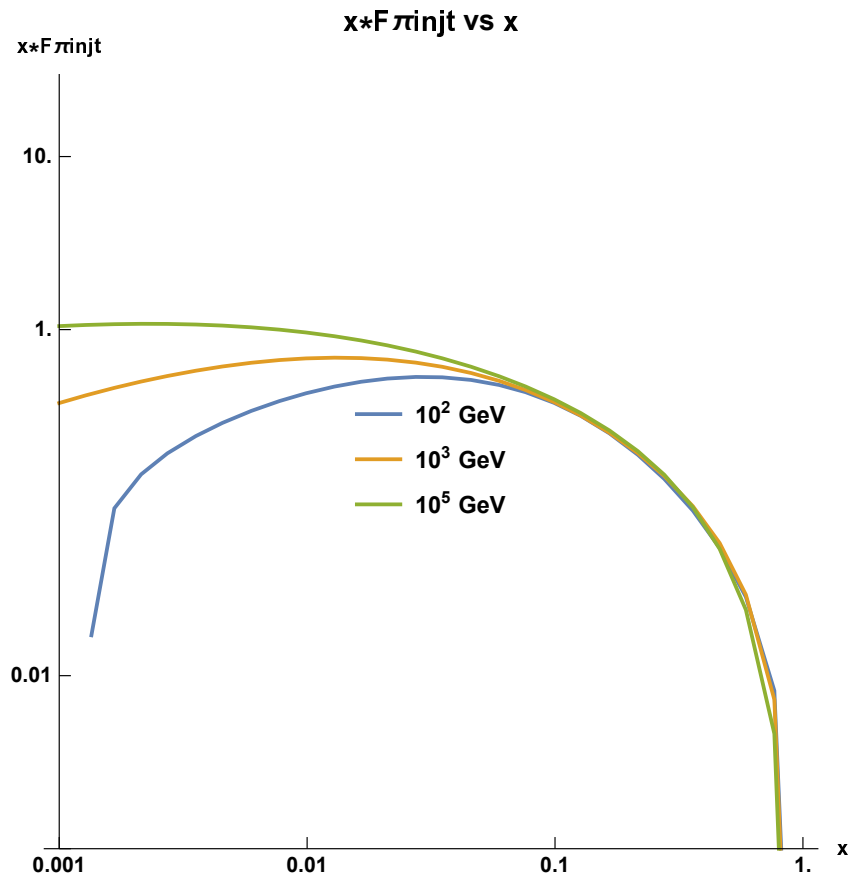
Figure 4: The F function, corresponding to the pion spectrum emerging from a single (hot-cold) proton collision, is presented here, multiplied by the x=$\frac{E_\pi}{Ep}$ fraction. The calculation is performed at three different energies for the non-thermal proton.

and

$$t_\pi = t_{\pi 0}\Gamma_\pi + t_{esc} \tag{6}$$

which in practice takes the form

$$t_\pi = t_{\pi 0}\left(\frac{E_\pi}{m_\pi c^2}\right) + t_{esc} \tag{7}$$

where the light escape time t_{esc} strongly affects the final result.

The synchrotron loss time scale is defined by

$$t_{sync}^{-1} = \frac{4}{3}\left(\frac{m_e}{m_p}\right)^3 \frac{1}{8\pi c m_e}\sigma_T B^2 \frac{E_p}{m_p c^2} \tag{8}$$

The form of the latter term, which is essentially Γ_p, facilitates energy-dependent calculations later-on. In total

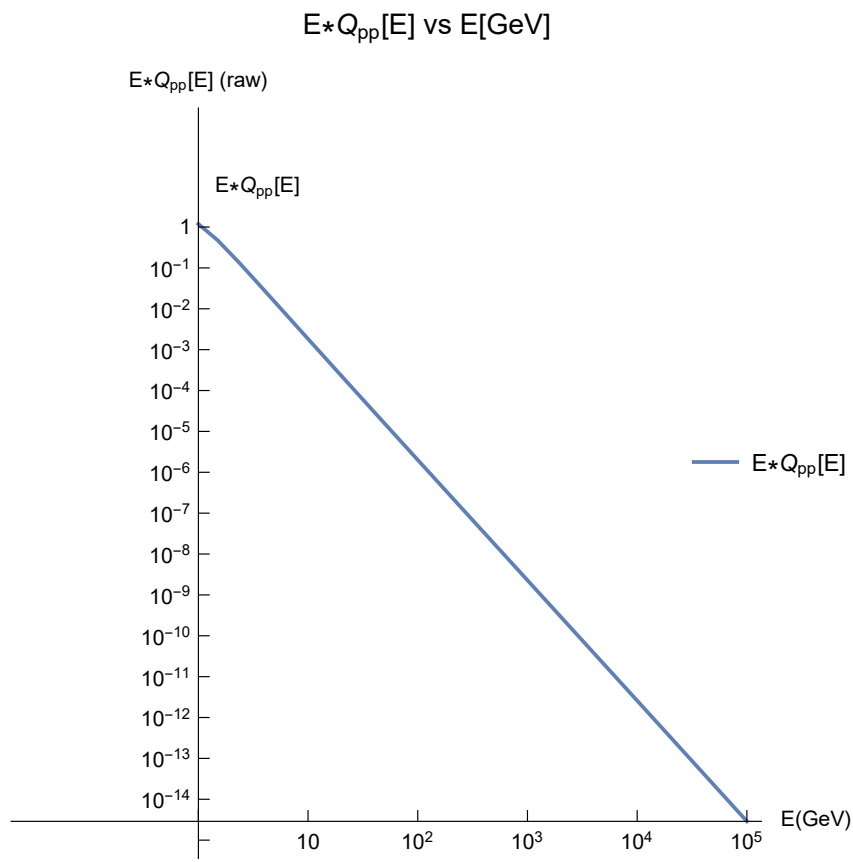$$t_{loss}^{-1} = t_{sync}^{-1} + t_{adb}^{-1} + t_{pp}^{-1} \tag{9}$$

6

Figure 5: The function Q, describing the combined spectrum from a multitude of (hot-cold) p-p collisions, spanning a range from 1 GeV to 100000 GeV.

3.2. A model for the interaction of thermal and non-thermal protons in the jet.

Hot-cold proton interaction results to a distribution of high energy pions, which then decay allowing the creation of energetic neutrinos. We have [17, 18, 19]

$$pp \rightarrow pp\pi^0 + \pi_0 \,, \tag{10}$$

for neutral pions π^0 and

$$pp \rightarrow pn\pi^+ + \pi_+ \,, \qquad pp \rightarrow pn\pi^- + \pi_- \,, \tag{11}$$

for $\pi^\pm$.

π^0 decay to gamma-rays, while $\pi^\pm$ mostly to an anti-muon or muon and a muonic neutrino or anti-neutrino (prompt neutrinos) [17].

$$\pi^+ \rightarrow \mu^+ + \nu_\mu \,, \qquad \pi^- \rightarrow \mu^- + \widetilde{\nu}_\mu \,. \tag{12}$$

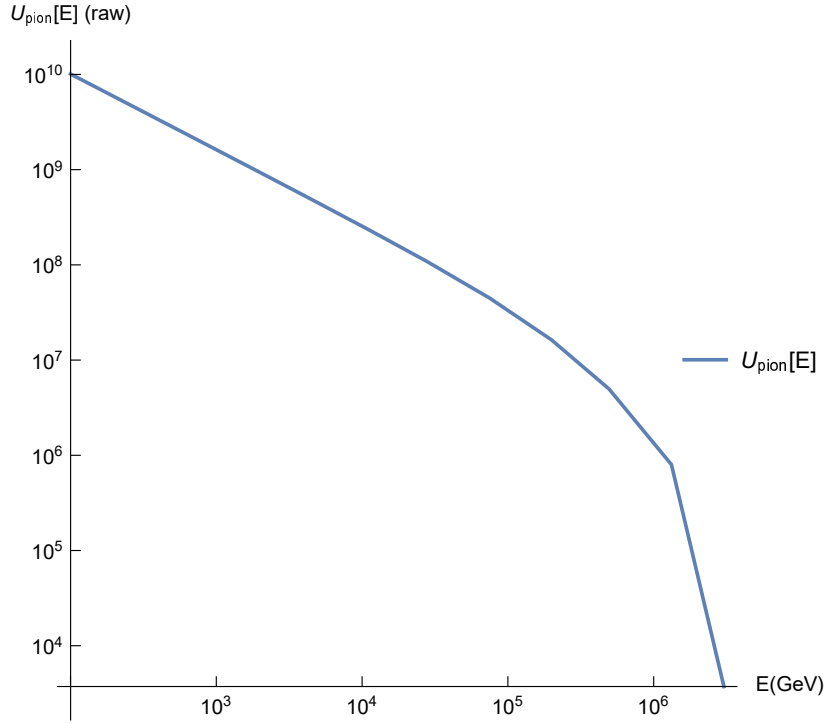As an approximation, we neglect both neutrino production through secondary channels and delayed neutrinos.

7

Figure 6: Pion energy distribution, plotted in non-normalized units vesrus energy.

For each succesive particle population in the above cascades, the transport
equation [20] can be solved. Nevertheless, for protons a power-law distribution
is assumed, skipping having to solve the first transport equation in the cascade.
From protons to pions then to muons and neutrinos, each generation of particles
leads to the next one. [12] calculate the properties of resulting particle distribu-
tions over a large energy range, performing Monte Carlo calculations with the
results of particle physics.

In previous works [19, 21, 22], the hadronic jet was modelled using the
PLUTO code. The results of PLUTO were then processed in order to cal-
culate the emissivity of γ-rays and neutrino using various approximations. In
this paper, the neutrino emmisivity is calculated separately at each spatial com-
putational cell, using the angle (los,u), formed between the LOS and the local
velocity.

3.3. Lorentz transform of high E proton distribution

For the calculation of the fast proton distribution, the relevant directional
equation is found in [23] [24]. The latest variant originates from [23], used here,
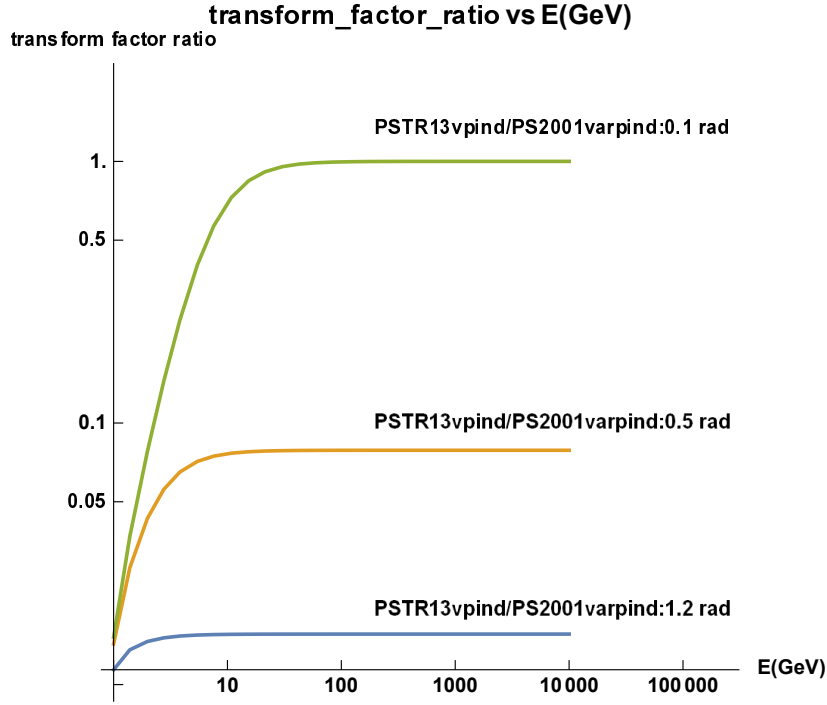
8

Figure 7: The ratio of TR13/PS01 HE proton distribution density transformation, for three different angles. A reproduction, for verification, of a figure from [23].

minus a geometry factor that we absorb into the normalization factor

$$n(E, \theta) = \frac{\Gamma^{-\alpha-1}E^{-\alpha}(1 - \beta cos(\theta)\sqrt{1 - \frac{m^2c^4}{E^2}})^{-\alpha-1}}{[sin^2(\theta) + \Gamma^2(cos(\theta) - \frac{\beta}{\sqrt{1-\frac{m^2c^4}{E^2}}})^2]^{\frac{1}{2}}} \tag{13}$$

On the other hand, [24] say

$$n(E, \theta) = \frac{\Gamma^{-\alpha+1}E^{-\alpha}(1 - \beta cos(\theta)\sqrt{1 - \frac{m^2c^4}{E^2}})^{-\alpha}}{[sin^2(\theta) + \Gamma^2(cos(\theta) - \frac{\beta}{\sqrt{1-\frac{m^2c^4}{E^2}}})^2]^{\frac{1}{2}}} \tag{14}$$

And a simpler variant [21]

$$n(E, \theta) = \Gamma(E - \beta\sqrt{E^2 - m^2c^4}cos(\theta)) \tag{15}$$

The above are plotted in Figures 7, 8 and 9.

3.4. Pion injection function and pion energy distribution

For each fast-slow proton interaction a spectrum of possible pion energies exists, given by the function F_π ([12], [5] and [6]).

9

transform_factor vs E(GeV)
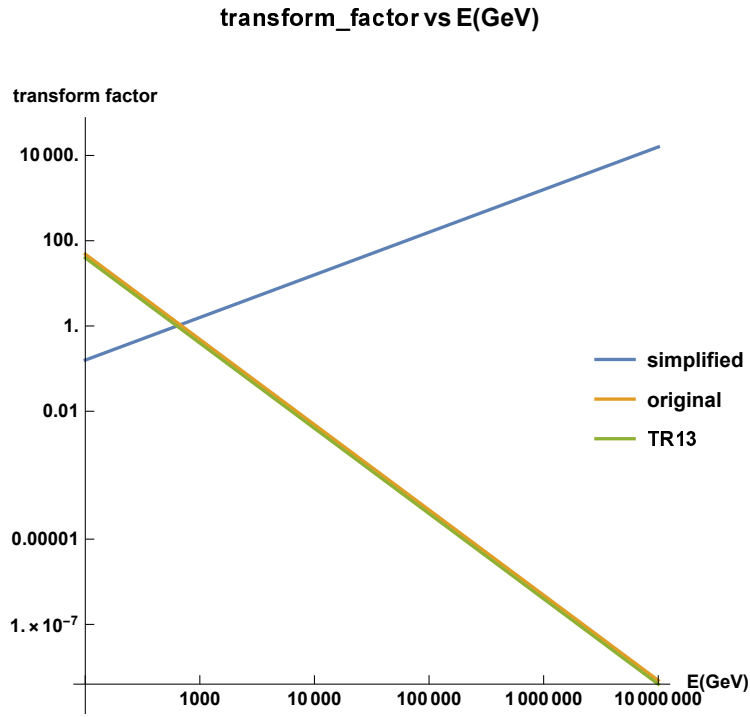
Figure 8: Three different expressions used for non-thermal proton distro transform, plotted with energy.

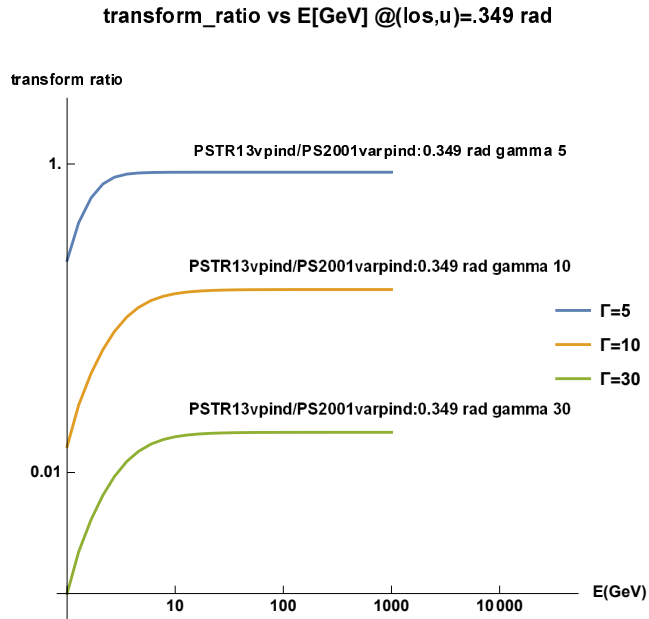**transform_ratio vs E[GeV] @(los,u)=.349 rad**

Figure 9: The ratio of TR13/PS01 non-thermal proton distribution density transformation, for three different Lorentz factors. A reproduction, for verification, of a figure from [23].

10

$$F_\pi^{(pp)}\left(x, \frac{E}{x}\right) = 4\alpha B_\pi x^{\alpha-1}\left(\frac{1-x^\alpha}{1+rx^\alpha(1-x^\alpha)}\right)^4 \tag{16}$$

$$\left(\frac{1}{1-x^\alpha} + \frac{r(1-2x^\alpha)}{1+rx^\alpha(1-x^\alpha)}\right)\left(1-\frac{m_\pi c^2}{xE_p}\right)^{\frac{1}{2}}$$

where $x = E/E_p$, and $L = ln(E_p/1000GeV)$, $E_{th} = 1.2$ GeV (see [5, 12]).

In Fig. 2 $\sigma_{pp}^{(inel)}$ is plotted. In Fig. 3 the p-law fast proton density is shown. In Fig. 4 xF_π is plotted with the fraction x for different fast proton energies.

The pion injection function, $Q_\pi^{(pp)}$, comprises, at each pion energy, pion contributions, to that pion energy, from the spectrum F, of all potential p-p interactions.

$$Q_\pi^{(pp)}(E,z) = n(z)c \int_{\frac{E}{E_p^{(max)}}}^{1} \frac{dx}{x}\left(\frac{E}{x}, z\right) F_\pi^{(pp)}\left(x, \frac{E}{x}\right) \sigma_{pp}^{(inel)}\left(\frac{E}{x}\right), \tag{17}$$

x is the fraction of the pion energy to proton energy, and $n(z)$ is the jet flow proton density.

In Fig 5 $Q_\pi^{(pp)}$ is plotted versus the pion energy E_π.

In order to obtain the pion distribution, we solve the following transport equation

$$\frac{\partial N_\pi}{\partial E} + \frac{N_\pi}{t_{loss}} = Q_\pi^{(pp)}(E,z) \tag{18}$$

where $N_\pi(E,z)$ denotes the pion energy distribution. We proceed

$$N_\pi(E) = \frac{1}{|b_\pi(E)|} \int_E^{E^{(max)}} dE' Q_\pi^{(pp)}(E') \exp\left[-\tau_\pi(E,E')\right], \tag{19}$$

where

$$\tau_\pi(E',E) = \int_{E'}^{E} \frac{dE'' t_\pi^{-1}(E)}{|b_\pi(E'')|}. \tag{20}$$

The above are performed for each computational cell, where quantities, for radiative purposes, are considered locally constant. A cell is macroscopically large,

11

inasmuch only the deterministic portion of the transport equation is employed, in turn rendering it deterministic. Again we take the characteristic scale (mean free path) of the radiative interactions to be smaller than the cell size, leading to the containment of particle interactions within a given hydrocode cell. Furthermore, the time scale for the radiative interactions is taken to be smaller enough than the hydrocode's timestep, that the radiative interactions belong to a single timestep each time.

3.5. Neutrino emissivity

The emissivity of prompt neutrinos [12, 13, 4, 5], is

$$
Q_{\pi \to \nu}(E) = \int_{E}^{E_{max}} dE_\pi t_\pi^{-1}(E_\pi) N_\pi(E_\pi) \frac{\Theta(1 - r_\pi - x)}{E_\pi(1 - r_\pi)} \, , \tag{21}
$$

$x = E/E_\pi$ and t_π is the pion decay timescale. $\Theta(\chi)$ is the theta function [5, 19]. Neutrino emissivity is calculated for each individual cell, using the cell's own angle to the LOS crossing that cell. The imaging process may either incorporate parallel LOS's or a focused beam, where each LOS follows a slightly different path to a common focal point [25]. A synthetic image of the model system is thus produced.

4. Results and discussion

4.1. Model setup

The jet base is situated near the centre of a Cartesian XYZ grid. A continuous model jet, representing a microquasar system, injected at u_{jet} =0.865c is studied with the RMHD setup of the PLUTO hydrocode, at a uniform grid resolution of $60 \times 100 \times 50$. In all of the model runs the same initial jet density of 10^{10} protons/cm^3 is used, 2000 times less than the maximum surrounding gas density. Winds comprise an accretion disk wind construct and a stellar wind, which falls off away from the companion star, located off-grid at (400, 100, 400), while the jet is threaded by a strong confining toroidal magnetic field of B=10^4
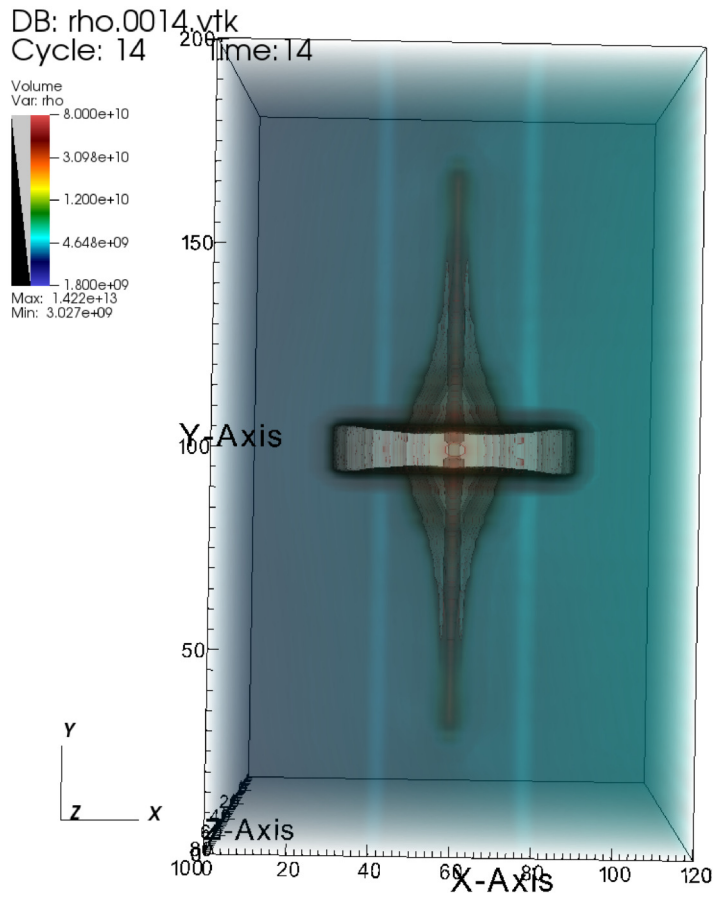
Figure 10: Snapshot 14 of the u=0.866c hydrocode run, corresponding to a model time of t=350 (14 × 25), depicting the density in a logarithmic plot. We can see both jet fronts advancing towards the ends of the grid, traversing the surrounding stellar wind, after crossing the simplified accretion disk wind construct. Image produced with VisIt.

G. The simulations were run until t = 842 s, saving a data snapshot every 25 time units. A snapshot of density is shown in Figures 10 and 11, in 3D and 2D respectively, where we can see the magnetically collimated jet pair advancing through surrounding winds.

A number of empty user parameters were fully employed, in order to house particle emission results later on. Then, the above PLUTO run was copied into many directories. In each one of them, the nemiss program [26] was run, that calculates neutrino emission for a specific imaging geometry and setup. The results were overwritten into the suitably prepared data files of the originally empty user parameters of the hydrocode.

A series of imaging geometries were employed: No 1 means parallel rays, projected onto the XZ plane, no 2 the same but onto the YZ plane, no 3 is focused rays, onto the XZ plane, and no 4 is focused rays onto the YZ plane.

13

| Parameter/Viewing Angle	0 deg	10 deg	30 deg	60 deg	D $\simeq$ 90 deg	Comments
cell size ($\times 10^{10} cm$)	2.0	2.0	2.0	2.0	2.0	PLUTO cell
ρ_{jet} (cm^{-3})	1.0×10^{10}	1.0×10^{10}	1.0×10^{10}	1.0×10^{10}	1.0×10^{10}	jet's matter density
ρ_w (cm^{-3})	1.0×10^{13}	1.0×10^{13}	1.0×10^{13}	1.0×10^{13}	1.0×10^{13}	max wind density
ρ_{dw} (cm^{-3})	2.0×10^{13}	2.0×10^{13}	2.0×10^{13}	2.0×10^{13}	2.0×10^{13}	max disk wind density
t_{run}^{max} (s)	842	842	842	842	842	model run time
Method	P. L.	P. L.	P. L.	P. L.	P. L.	Piecewise Linear
Integrator	M. H.	M. H.	M. H.	M. H.	M. H.	MUSCL-Hancock
EOS	Ideal	Ideal	Ideal	Ideal	Ideal	Equation of state
BinSep (cm)	4.0×10^{12}	4.0×10^{12}	4.0×10^{12}	4.0×10^{12}	4.0×10^{12}	Binary separation
$M_{BH}/M_{\odot}$	3-10	3-10	3-10	3-10	3-10	VE compact star mass
$M_{\star}/M_{\odot}$	10-30	10-30	10-30	10-30	10-30	Companion mass
$\beta = v_0/c$	0.866	0.866	0.866	0.866	0.866	Initial jet speed
L_k^p	$2.5 * 10^{38}$	$2.5 * 10^{38}$	$2.5 * 10^{38}$	$2.5 * 10^{38}$	$2.5 * 10^{38}$	Jet kinetic luminocity
grid resolution	60*100*50	60*100*50	60*100*50	60*100*50	60*100*50	PLUTO grid size (xyz)
imaging method	FB	PR	PR	PR	FB	focused beam or parallel rays
time delay	off	off	off	off	off	very high LOS speed
imaging plane	XZ-screen	XZ/YZ	XZ/YZ	XZ/YZ	YZ-screen	box side or inner screen

Table 1: Table of run data
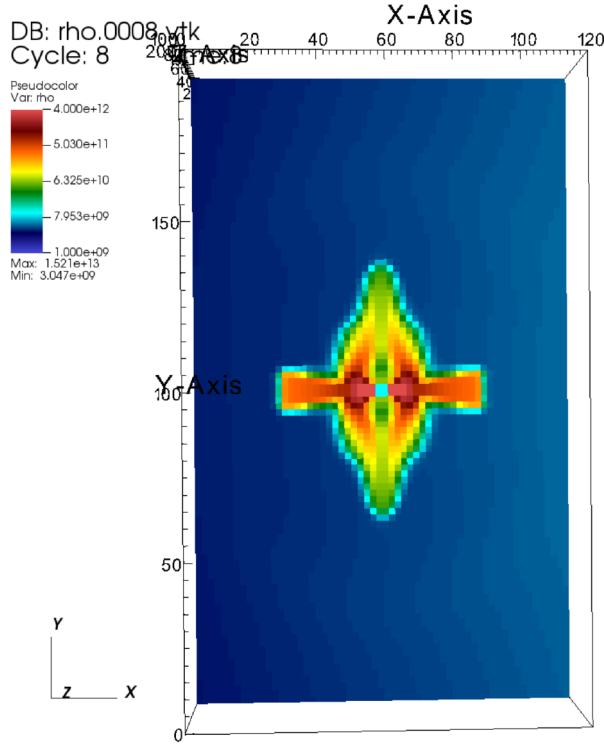
Figure 11: Snapshot 8 of the u=0.866c hydrocode run, corresponding to a model time of t=200 (8 × 25), depicting a slice of the density in a logarithmic plot. The slice is cut along the jet. We can see both jet fronts traversing the stellar wind of the companion, after emerging from the model disk wind. Image produced with VisIt.

Three different angles were employed for the cases 1 and 2, while for cases 3 and 4 the respective focal points imply near-head-on and sidereal views.

145   Rlos2 [25] was then run, using the combined PLUTO-nemiss data, with sfactor=1 for the pload shrink factor. In general, the imaging process may or may not use all snapshots available to it, depending on the light crossing time of its model segment (adjusted through the clight parameter in rlos2). Trying to read more snapshots than loaded corrupts the hydrocode time array of rlos2, 150 called T, resulting to errors. For simplicity, in our case an artificially very high clight was used, in order to effectively switch off the time-delay effect. A double filter was used for velocity and for los,u angle. A minimum velocity and a maximum angle were set, in order to trigger the calculation of the neutrino emission for a particular cell. This way, the expensive part of the simulation 155 was only performed where it was really worth it. This alleviated in part the discrepancy between computational costs of the dynamic and the radiative parts

15

of the model.

An important aspect of this modelling approach is that each cell has a different emissivity visible from Earth, than its neighbors. That is because each cell may differ from the next one in terms of both speed and orientation to us. This combination means that, in general, the hydro model gives different results than the steady-state one. A vortéx with relativistic velocities, for example, may in part appear very luminous, where it is fast with local speed pointing towards us, and also too dark, where velocities point away from us. In this simulation, such effects were limited, but at a higher resolution, it is expected than non-linear dynamic effects in the hydrocode shall interact profoundely with the radiative part of the model.

The scale of the total emission increases the closer the LOS gets to the jet pair axis Figures 12 and 13. The low resolution employed did not allow for significant non-linear dynamic effects to appear, yet the concept of the modelling process was proven to work in its entirety. On the other hand, the normalization process demonstrates the possibility of potential observations, as the results potentially fall within the detection range of contemporary arrays [5].

A series of both dynamical and imaging parameters may be adjusted, in order to cover different scenario. The suite works in a highly automated manner, and is prepared to take on high resolution applications. There, the relativistic effects of non-linear dynamics shall appear in full.

5. Final remarks

Particle emission from a typical microquasar was simulated using a suitable program suite. The results verified the integrity of the process, opening the way for more detailed runs in the future.

References

[1] I. F. Mirabel, L. F. Rodríguez, Ann. Rev. Astron. Astrophys37 (1999) 409.
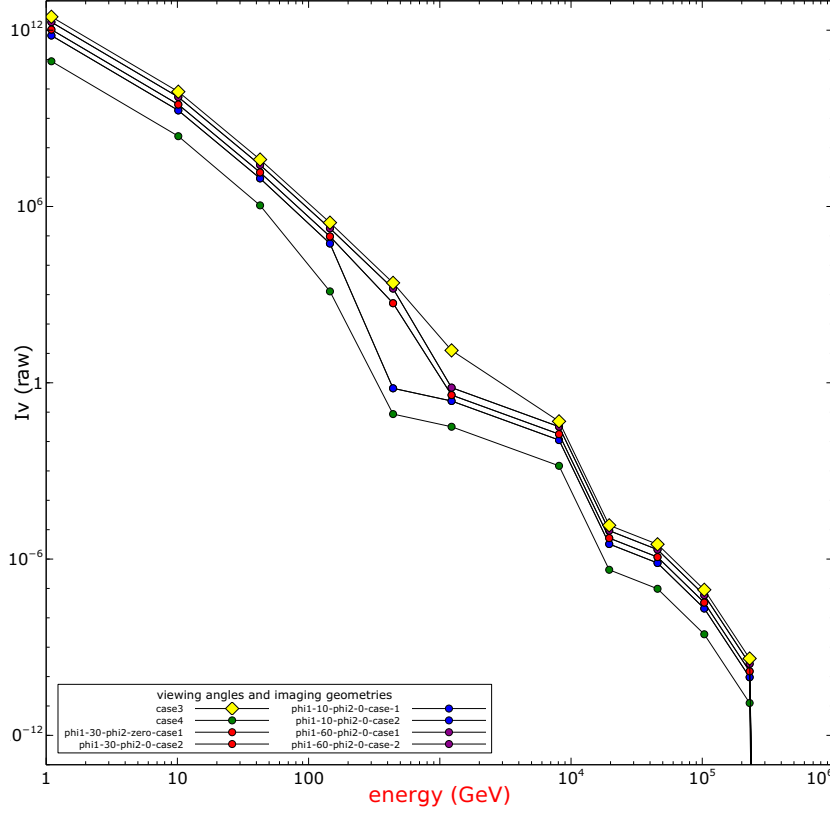
16

Figure 12: Non-normalized SED from a series of radiative simulations, based on the same RMHD dynamic model run. We can see the intensity dropping as the angle of observations deviates from the jet pair axis. Image produced with veusz, using data produced with PLUTO, rlos2 and nemiss.

[2] G. E. Romero, D. F. Torres, M. M. Kaufman Bernadó, I. F. Mirabel, Hadronic gamma-ray emission from windy microquasars, Astron. & Astrophys.410 (2003) L1–L4. `arXiv:astro-ph/0309123`, `doi:10.1051/0004-6361:20031314-1`.

[3] W. Bednarek, TeV Neutrinos from Microquasars in Compact Massive Binaries, Ap. J.631 (1) (2005) 466–470. `arXiv:astro-ph/0505547`, `doi:10.1086/432411`.

[4] M. M. Reynoso, G. E. Romero, H. R. Christiansen, Production of gamma rays and neutrinos in the dark jets of the micro-
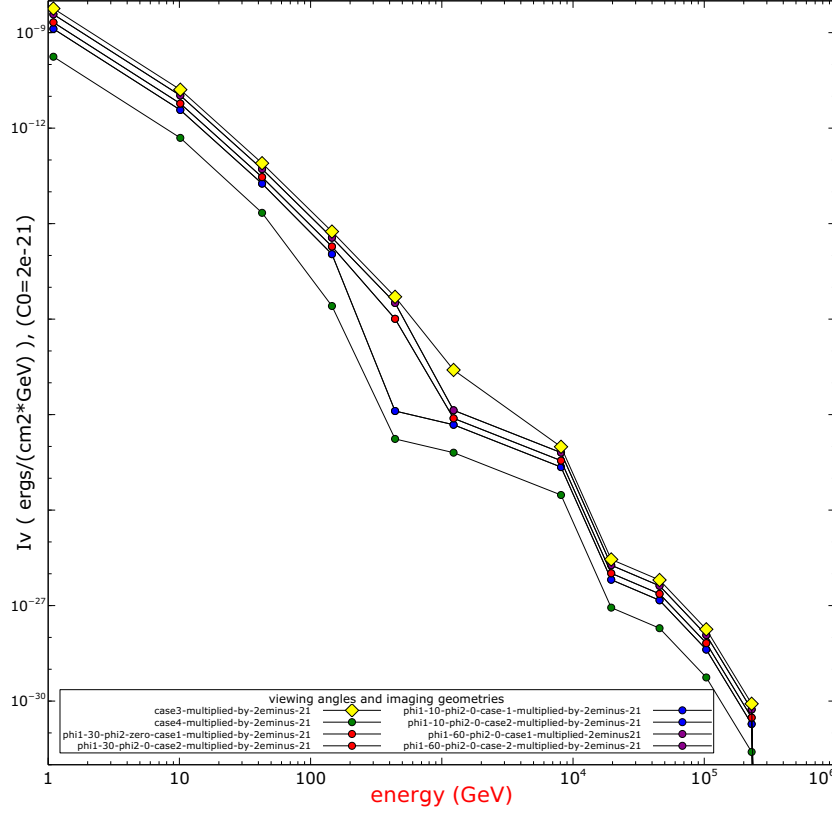
17

Figure 13: Normalized SED from a series of radiative simulations, where comparisons with potential observations are made possible. See the Appendix for more details on the normalization process. Data finally processed and image produced with veusz.

quasar SS433, MNRAS387 (4) (2008) 1745–1754. `arXiv:0801.2903`, `doi:10.1111/j.1365-2966.2008.13364.x`.

[5] M. M. Reynoso, G. E. Romero, Magnetic field effects on neutrino production in microquasars, Astron. & Astrophys.493 (1) (2009) 1–11. `arXiv:0811.1383`, `doi:10.1051/0004-6361:200811004`.

[6] M. M. Reynoso, A. M. Carulli, On the possibilities of high-energy neutrino production in the jets of microquasar SS433 in light of new observational data, Astroparticle Physics 109 (2019) 25–32. `arXiv:1902.03861`, `doi:10.1016/j.astropartphys.2019.02.003`.

[7] D. Koessl, E. Mueller, W. Hillebrandt, Numerical simulations of axially symmetric magnetized jets. I - The influence of equipartition magnetic fields. II - Apparent field structure and theoretical radio maps. III - Collimation of underexpanded jets by magnetic fields, Astron. & Astrophys.229 (2) (1990) 378–415.

[8] F. M. Rieger, P. Duffy, A Microscopic Analysis of Shear Acceleration, Ap. J.652 (2) (2006) 1044–1049. `arXiv:astro-ph/0610187`, `doi:10.1086/508056`.

[9] F. M. Rieger, An Introduction to Particle Acceleration in Shearing Flows, Galaxies 7 (3) (2019) 78. `arXiv:1909.07237`, `doi:10.3390/galaxies7030078`.

[10] Singh2019MHD, Study of relativistic magnetized outflows with relativistic equation of state, Monthly Notices of the Royal Astronomical Society 488 (4) (2019) 5713–5727. `arXiv:https://academic.oup.com/mnras/article-pdf/488/4/5713/29191239/stz2101.pdf`, `doi:10.1093/mnras/stz2101`.
URL `https://doi.org/10.1093/mnras/stz2101`

[11] S. Fabrika, The jets and supercritical accretion disk in SS433, 12 (2004) 1–152. `arXiv:astro-ph/0603390`.

[12] S. R. Kelner, F. A. Aharonian, V. V. Bugayov, Energy spectra of gamma rays, electrons, and neutrinos produced at proton-proton interactions in the very high energy regime, Phys. Rev. D74 (3) (2006) 034018. `arXiv:astro-ph/0606058`, `doi:10.1103/PhysRevD.74.034018`.

[13] P. Lipari, M. Lusignoli, D. Meloni, Flavor composition and energy spectrum of astrophysical neutrinos, Physical Review D 75 (12). `doi:10.1103/physrevd.75.123005`.
URL `http://dx.doi.org/10.1103/PhysRevD.75.123005`

[14] M. C. Begelman, R. D. Blandford, M. J. Rees, Massive black hole

binaries in active galactic nuclei, Nature287 (5780) (1980) 307–309. `doi:10.1038/287307a0`.

[15] P. A. Hughes, in: Hughes (Ed.), Beams and Jets in Astrophysics, Cambridge University Press, 1991.

[16] E. V. Derishev, F. A. Aharonian, V. V. Kocharovsky, High-energy emission from off-axis relativistic jets, in: F. A. Aharonian, H. J. Völk, D. Horns (Eds.), High Energy Gamma-Ray Astronomy, Vol. 745 of American Institute of Physics Conference Series, 2005, pp. 510–515. `arXiv:astro-ph/0501197, doi:10.1063/1.1878454`.

[17] O. Kosmas, T. Smponias, aHEP accepted (2018).

[18] T. Smponias, O. Kosmas, Advances in High Energy Physics 4962741.

[19] T. Smponias, O. Kosmas, Advances in High Energy Physics 921757.

[20] W. R. M. James J. Duderstadt, Transport theory, Wiley, New York, 1979.

[21] T. Smponias, T. S. Kosmas, MNRAS438 (2014) 1014.

[22] T. Smponias, T. S. Kosmas, MNRAS412 (2011) 1320.

[23] D. F. Torres, A. Reimer, Hadronic beam models for quasars and microquasars, Astron. & Astrophys.528 (2011) L2. `arXiv:1102.0851, doi:10.1051/0004-6361/201116488`.

[24] D. Purmohammad, J. Samimi, On the hadronic beam model of TeV gamma-ray flares from blazars, Astron. & Astrophys.371 (2001) 61–67. `doi:10.1051/0004-6361:20010308`.

[25] T. Smponias, RLOS: Time-resolved imaging of model astrophysical jets (Nov. 2018). `arXiv:1811.009`.

[26] T. Smponias, nemiss: neutrino imaging of model astrophysical jets (Nov. 2019).

[27] D. Weiskopf, Dissertation, Ph.D. thesis, Dissertation, der Eberhard-Karls-Universitat zu Tubingen, der Fakultat fur Physik (2001).

[28] T. V. Cawthorne, in: Hughes (Ed.), Beams and Jets in Astrophysics, Cambridge University Press, 1991.

[29] W. B. Sparks, D. Fraix-Burnet, F. Macchetto, F. N. Owen, A counterjet in the elliptical galaxy m87, Nature 355 (1992) 804.

[30] R. Laing, A. H. Bridle, Relativistic models and the jet velocity field in the radio galaxy 3c 31, Monthly Notices of the Royal Astronomical Society 336 (2002) 328.

[31] R. M. Hjellming, K. J. Johnston, ApJ 328 (1988) 600.

[32] A. Mignone, G. Bodo, S. Massaglia, T. Matsakos, O. Tesileanu, C. Zanni, A. Ferrari, Ap. J. Supp.170 (2007) 228.

6. Appendix 1

6.1. Normalization

The kinetic energy of the jet at its base can be expressed as

$$E_k = \frac{1}{2}(\Gamma m)u^2 \tag{22}$$

where u is the jet speed, and m the mass of a jet portion crossing the cross section of the jet there. Then, the jet kinetic power, is the kinetic energy traversing the cross section per unit time

$$P_k = dE_k/dt = \frac{1}{2}(\Gamma dm/dt)u^2 \tag{23}$$

where the speed is taken constant during an ejection episode (it is also set constant in the simulation described here). But

$$dm/dt = \rho dV/dt = \rho A dx/dt = \rho A u \tag{24}$$

where A is the jet base cross section area, also taken constant both in the simulation and here. Therefore

$$P_k = dE_k/dt = \frac{1}{2}(\Gamma\rho A)u^3 \qquad (25)$$

or

$$P_k = dE_k/dt = \frac{1}{2}(\Gamma\rho N_{cell}L_{cell}^2)u^3 \qquad (26)$$

where $A = N_{cell}L_{cell}^2$. L_{cell}^2 is the area of the side of length L_{cell} of a cubical computational cell, at the jet base, and N_{cell} is the number of such cells forming the jet base. We then express density as a function of proton number density N_p and proton mass m_p

$$\rho = N_p m_p. \qquad (27)$$

Furthermore, we introduce a factor $\alpha = L_\nu/L_k$, representing the portion of jet power emitted in neutrinos. A typical value is taken as 10^{-3}. We also set u=βc. A less than unity, positive filtering factor f_f is employed, which accounts for not using all of the jet cells, but only those with velocity orientation closer to the LOS and also with speed above a given limit.

We then have

$$L_\nu = \alpha L_k = \alpha P_k = \alpha dE_k/dt = f_f \frac{1}{2}\alpha\Gamma(N_p m_p N_{cell}L_{cell}^2)\beta^3 c^3 \qquad (28)$$

The intensity of the jet is then expressed as $I_\nu = L_\nu/4\pi D^2$, where D is the distance to Earth. Thus

$$I_\nu = f_f \frac{1}{4\pi D^2}\alpha\frac{1}{2}\Gamma(N_p m_p N_{cell}L_{cell}^2)\beta^3 c^3 \qquad (29)$$

In our simulation, the jet beam travels at $\beta=\frac{u}{c}$ =0.866, with a density of 10^{10} protons/cm^3. L$_{cell}$ is 10^{10} cm, while the number of cells comprising the beam, at its base, at this resolution, is N$_{cell} \simeq 15$. Γ=2. The distance to Earth, is taken here with a typical value of D=5 kpc, or approximately 2$\times$ 10^{22} cm.

We then integrate the area under the curve of the arbitrary units plot, for the case of nearly non-beamed data, at ϕ_1=10 degrees. That case is supposed, for the purposes of normalization, to be the one matching the orientation of

22

the hypothetical system in relation to Earth. We do a cumulative sum over the roughly ten points, admitting a ten percent coverage per order of magnitude scale level. Thus, we find about 10^{11}, which means that our sum is ten times smaller, or approximately 10^{10}, in arbitrary units (AU)*GeV. We replace an AU with a constant C_0, so that AU= C_0 erg/(s*cm^2).

We set $I_\nu = L_\nu/4\pi D^2$ equal to the area under the plot, expressed in units of C_0, in order to find the latter (normalization constant)

$$I_\nu = f_f \frac{1}{4\pi D^2} \alpha \frac{1}{2} (\Gamma(N_p m_p) N_{cell} L^2_{cell}) \beta^3 c^3 = (PLOT AREA) * C_0 erg/(scm^2) GeV \tag{30}$$

For our case, we find $C_0 \simeq 2* 10^{-21}$, which is the value of the arbitrary unit C_0. Using the above constant, we multiply by it the value given in arbitrary units for the particle emission. Thus the intensity plot is multiplied, and we arrive to the updated plot in Figure 13, which may be directly compared to other models and to observations.

7. Appendix 2

The equipartition calculation now follows. As shown above, the jet kinetic power is

$$L_k = \frac{1}{2} \frac{dm}{dt} u^2 = \frac{1}{2}(\rho A u) u^2 = \frac{1}{2} \rho A u^3 \tag{31}$$

where $\frac{dm}{dt} = \rho \frac{dV}{dt} = \rho A \frac{dx}{dt} = \rho A u$

The kinetic energy density is [5]

$$\rho_k = \frac{L_k}{\pi R_j^2 u_j} = \frac{L_k}{Au} = \frac{\frac{1}{2}\rho A u^3}{Au} = \frac{1}{2}\rho u^2 \tag{32}$$

which also acts as verification.

We also have

$$B = \sqrt{8\pi \rho_B} \tag{33}$$

For equipartition, we set the kinetic and magnetic energy densities equal to each other, $\rho_k = \rho_B$. So

$$B = \sqrt{8\pi \rho_B} = \sqrt{8\pi \rho_k} \tag{34}$$

23

We can now have ρ_k and then we shall calculate the B that corresponds to equipartition for that. Our beam has $\rho=10^{10}\text{cm}^{-3}$, or about 1.6×10^{-14} gcm^{-3}. So

$$\rho_k = \frac{1}{2}(1.6 \times 10^{-14}\frac{g}{cm^3})(\frac{\sqrt{3}}{2}3 \times 10^{10}\frac{cm}{s})^2 \simeq 5.4 \times 10^6 \frac{g}{cms^2} \qquad (35)$$

Therefore, in CGS

$$B = \sqrt{8\pi\rho_k} \simeq \sqrt{8\pi\ 5.4 \times 10^6} \simeq 11.5 \times 10^3 \qquad (36)$$

For our simulation we set a rounded value of B=10^4 G, which is not far from the approximate equipartition value found above.

—————————————————————————————— SOS   inquire   about flow D

also inquire about an rlos2 appendix, send a second version with it attached SOS

8. Appendix 3

The RLOS special relativistic imaging program is described here.

8.1. Relativistic Effects

The main effects of the Lorentz/Poincaré transform on the emission from a relativistic object [27], specifically applied to an astrophysical jet, are relativistic aberration, time dilation and frequency shift [28, 15, 29, 30].

8.1.1. Lorentz factor

The Lorentz factor for a hydrocode cell is [15]

$$\Gamma_{Lorentz} = \frac{1}{\sqrt{1 - u^2}} \qquad (37)$$

where

$$u = \sqrt{u_x^2 + u_y^2 + u_z^2} \leq 1 \qquad (38)$$

is the value of the local velocity $\vec{u} = (u_x, u_y, u_z)$, in units of the speed of light.

24

8.1.2. Doppler factor calculation

Jet radiation is either boosted or de-boosted, depending on the angle losu, between the direction of the LOS and $\vec{u}$. The higher the jet speed, the narrower and stronger the cell boost cones around the jet head direction. On the other hand, outside cell boost cones, *de*-boosting occurs, that is to say the higher the velocity is, the weaker the signal becomes. D equals

$$D = \frac{\sqrt{1-u^2}}{(1-u*cos(losu))} \tag{39}$$

For both the above equations, the angle between the LOS and the local velocity vector is required at every point of the computational space.

For particles, the their distribution is transformed to the Earth frame, as shown in [23].

The cosine of angle losu is calculated in the following manner:

Let us define a fiducial unitary LOS vector $(L\vec{O}S) = (lx_1, lx_2, lx_3)$, with $(LOS) = \sqrt{lx_1^2 + lx_2^2 + lx_3^2} = 1$. In the following, ϕ_1 and ϕ_2 represent azimuth and elevation angles 1 and 2, respectively.

$$lx_1 = cos(\phi_1)cos(\phi_2), \ lx_2 = sin(\phi_1)cos(\phi_2), \ lx_3 = sin(\phi_2) \tag{40}$$

$$L\vec{O}S * \vec{u} = (LOS)*u*cos(\widehat{L\vec{O}S, \vec{u}}) = L\vec{O}S * \vec{u} = lx_1*u_x + lx_2*u_y + lx_3*u_z \tag{41}$$

Therefore, we have ((LOS)=1)

$$cos(\widehat{L\vec{O}S, \vec{u}}) = \frac{lx_1 * u_x + lx_2 * u_y + lx_3 * u_z}{(LOS) * u} = \frac{lx_1 * u_x + lx_2 * u_y + lx_3 * u_z}{\sqrt{(u_x^2 + u_y^2 + u_z^2)}} \tag{42}$$

A miniscule number is added to the denominator of equation 42, in case u=0. The above calculation allows the assignement of a Doppler boosting factor, through equations 38, 39 and 42, to each discrete emission event along a line of sight.

8.1.3. Doppler boosting

This area refers to electromagnetic emissions, but not to particle emission.

25

The jet spectrum is given by any suitable form inserted into the model. Earth frame jet spectrum S_{obs} can be expressed [15, 28] as

$$S_{obs} = S_{jet}D^{3+\alpha} \tag{43}$$

where α is the spectral index. The exponent $(3+\alpha)$ in the above can be broken down into different contributions from separate effects. Two units come from the aberration of light, one from the relativistic dilation of time and α from the effect of frequency shift, while for a continuous optically thin jet a D factor is lost [28].

Aberration-searchlight effect. Relativistic aberration changes the perceived direction of light (there is no curving in Special Relativity), when transforming between the jet frame and the earth frame, 'tilting rays', emanating from the jet, generally towards its head area.

Cell emission along a ray *within* the cell's boost cone, is then reinforced accordingly, while if *outside* the cone it is weakened. Depending on the local velocity value and direction, succesive or neighbouring cells may have totally different boost cones.

Time dilation. Time dilation contributes one D factor to the emission result. Again, this refers to E/M radiation.

8.2. 3-dimensional imaging

The 3D setup of RLOS emulates that of its ancestor classical imaging code ([22, 21, 17]). From each pixel of the "imaging" side, of the 3D computational domain (Figure 14), a line of sight (LOS) is drawn, through the imaged volume. Along the LOS, the equation of radiative transfer is solved at each cell, using local emission and absorption coefficients. Depending on the situation modelled, coefficients may either be calculated directly, or outsourced to another program.

Lines of sight are drawn, starting from a pixel of the yz-side or xz-side (either way called the imaging side) of the domain, tracing their way along the given direction (Figures 14 and 15), until they reach a length of
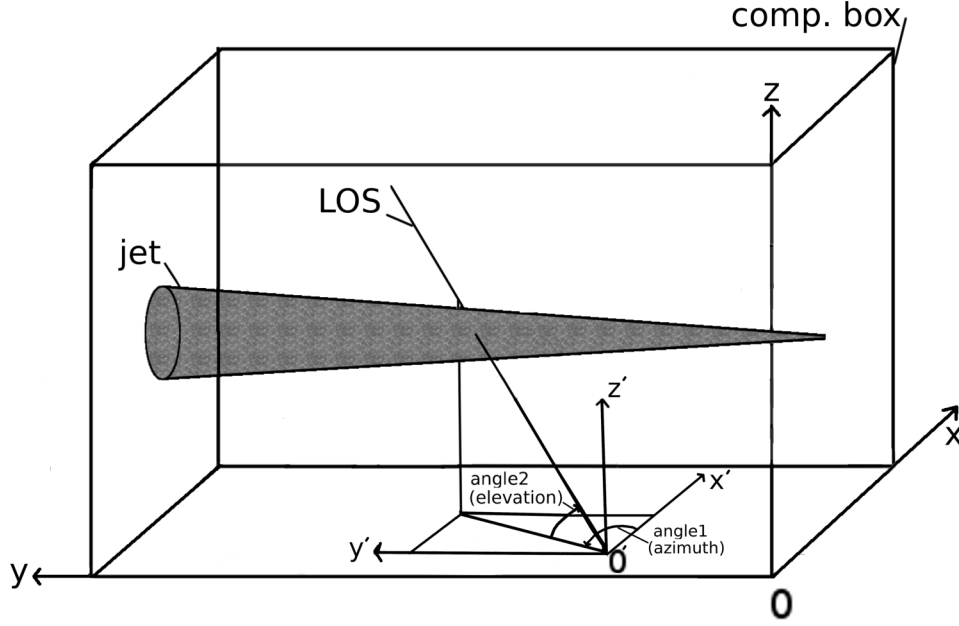
26

Figure 14: A 3D schematic view, of RLOS applied to a model astrophysical jet. The imaging side of the computational box is the yz plane, located on the side of the box apparently closer to the reader. Lying on the yz plane, O′ is the point of origin of a random LOS, with its own dashed coordinate system x′y′z′. Alternatively, the imaging plane may also lie on the xz side of the box. The final image is taken to formed on the eye or detector of a fiducial observer, situated at the end of the LOS.

$\sqrt{(x_{max}^2 + y_{max}^2 + z_{max}^2)}$, where $x_{max}, y_{max}, z_{max}$ are the dimensions, in cells, of the computational domain. In practice, on reaching the ends of the domain a LOS calculation halts, therefore some LOS's end up shorter than others. The above process is repeated within a 2D loop, running over the imaging plane, each LOS corresponding to a single pixel of the final synthetic image. Along a LOS, no sideways scattering is considered SOS 290319 DIG UP REF for that cos ref2 asked why no scsttering? SOS.

A model astrophysical system may be inserted into RLOS directly, for example forming a 'conical' jet setup [31]. Alternatively, data output from a hydrocode may be employed, which is the case in the current paper, using PLUTO [32].

27

8.3. Time-resolved imaging

8.3.1. Accessing 4-dimensional data

The finite nature of the speed of light affects the appearance of a fast-moving object in a crucial manner. Consequently, drawing a relativistic image of an astrophysical system, necessitates the availability of information regarding not only its spatial properties, but its temporal evolution as well. In our case, when executing the hydrocode, before running RLOS, we adjust the temporal density of snapshots, to be saved to disk at regular intervals. The smaller those intervals, the better the temporal resolution of hydrocode data. A series of snapshots shall then be loaded to RAM by RLOS, which therefore requires a multiple quantity of memory, in order to run properly, than the hydrocode itself. Time is measured in simulation time units, which are read by PLUTO's attached 'pload.pro' routine, which loads data into RLOS.

The total time span available to a LOS, $\Delta t_{LOS(total)} = t_{(last-shot)} - t_{(first-shot)}$ [1] (as measured in simulation time units, *not* merely in number of snapshots), should be preset to be larger than the light crossing time of the model system, at the selected LOS angle settings. Documenting the model jet evolution generally requires hydrocode data saves to be rather dense in time, especially for fast-changing flows. On the other hand, a lower temporal resolution will probably suffice for a steadier, slower-paced flow.

8.3.2. Traversing the 4D arrays

Introduction. A series of hydrocode snapshots are loaded to RAM, populating the elements of 4-dimensional (4D) arrays. From a *temporal* point of view, we begin from the simulation time corresponding to the first of the loaded snapshots, called shotmin. From a *spatial* point of view, we start at the first point of the imaging plane, which is a side of the computational box (Figure 14). As the calculation advances, in 3D space, along the LOS being drawn (Figure 15), the algorithm keeps checking whether to jump to a new *temporal* slice,

---

[1]Not to be confused with the interval Δt_{shot} between *successive* snapshots
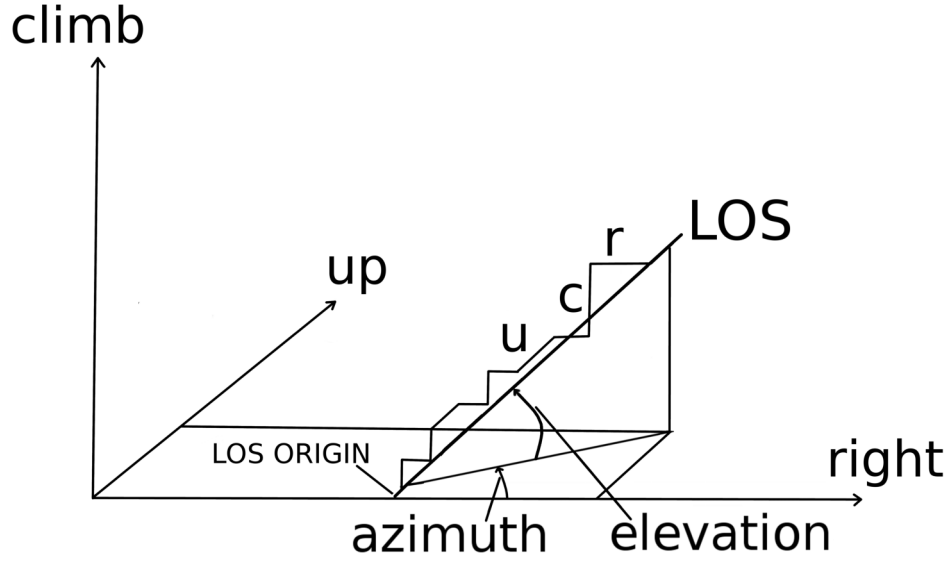
Figure 15: A schematic of the spatial propagation of the line of sight (LOS) through the 3D Cartesian computational grid. In the discrete grid, according to the design of the algorithm, there are 3 available directions to be taken at each step along the LOS: *right*, *up* and *climb*. These correspond to x, y and z, respectively. During propagation, the LOS 'tries' to follow its given direction, as defined by the two angles of azimuth and elevation. More specifically, every two steps a decision if first made on azimuth, either right or up. Then, for elevation, it is either climb, or another azimuth decision. In the Figure, along the LOS, horizontal steps point to the 'right' direction. Diagonal steps represent going 'up', while vertical ones constitute 'climb' steps.

385 while staying 'on target' in 3D (Figure 16). Consequently, the LOS advances in time, through data (Figure 17), by accessing succesive instants from the 4D data arrays.

Time-resolved imaging calculations. For every LOS, there is a point of origin (POO), located on the "imaging side" of the computational grid (Figure 14).

390 That point, addressed in the code as (nx10, ny10, nz10) and here as O', is the beginning of the LOS's axes x', y', z', parallel to x, y, z respectively. A 2D loop covers the imaging surface, the POO successively locating itself at each of the latter's points.
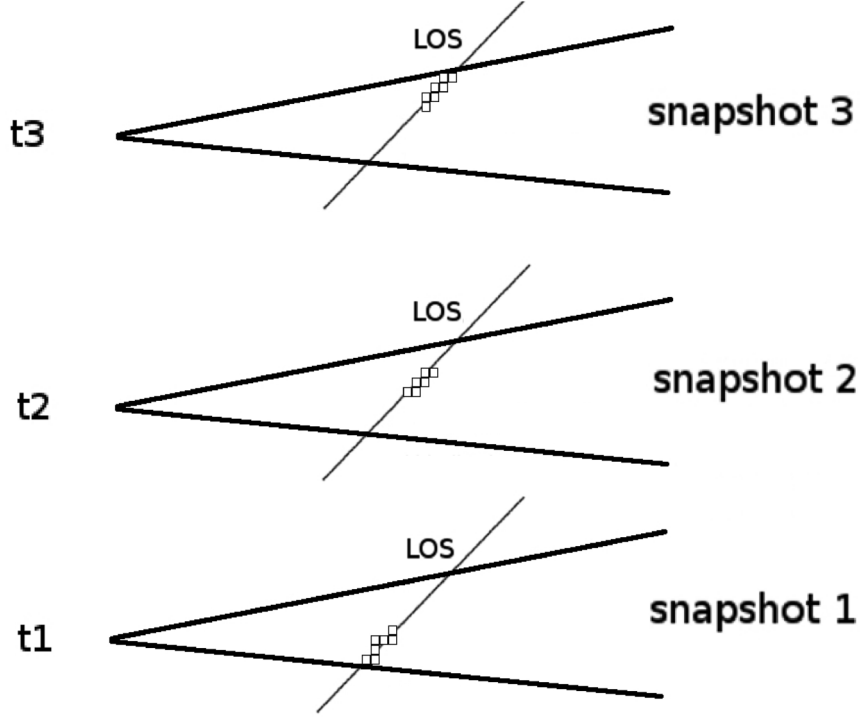
Figure 16: Three successive instants of a line of sight traversing a jet. At regular intervals, we jump to a new 3D slice of a 4D spacetime array, obtaining a discrete approximation of the time continuum, in the form of hydrocode snapshots.

As we progress along a LOS, a record is kept of where we are, in 3D space. This record comprises the LOS's own integer coordinates, rc, uc, and cc, measured, in cells, from its POO. The above symbols stand for right-current, up-current and climb-current, representing the current LOS advance in the x′, y′ and z′ axes, respectively (Figures 14 and 15). The current ray position is then (nx10+rc, ny10+uc, nz10+cc).

A timer variable, curtime (standing for current LOS time), is introduced for each LOS, recording the duration of insofar ray travel along the LOS. The aforementioned timer is preset at the beginning of each LOS, to the hydrocode time of the first loaded data snapshot.

We then proceed to calculate the current length of the LOS

$$l_{los(current)} = [(dlr * (nx1current - nx10))^2 +$$

$$(dlu * (ny1current - ny10))^2 + (dlc * (nz1current - nz10))^2]^{1/2} \qquad (44)$$

where the LOS length is measured in cell length units and

$$nx1current = nx10 + rc, \ ny1current = ny10 + uc, \ nz1current = nz10 + cc$$
$$(45)$$

Along the x, y and z directions, dlc, dlu, dlr are the respective *normalized* hydrocode cartesian cell lengths. Their values are usually unity, or close to unity, as set in the hydrocode by the user, and RLOS requires them fixed, meaning only homogeneous grids are currently supported. Furthermore, if the hydrocode grid is read, by pload, at a reduced resolution, then RLOS cell sizes are automatically adjusted accordingly.

We can finally write

$$l_{los(current)} = [((dlr * rc)^2) + ((dlu * uc)^2) + ((dlc * cc)^2)]^{1/2} \qquad (46)$$

We then proceed to calculate curtime, the current hydro simulation time of the light ray along the LOS.

$$curtime = l_{los(current)}/c_{light} + t_{0(LOS)}. \qquad (47)$$

$t_{0(LOS)}$ is the timestamp of the first loaded snapshot, when the LOS begins to be drawn, from its point of origin, and clight is the speed of light, in cells per simulation second.

When curtime exceeds the next snapshot's timetag, the algorithm switches to drawing the LOS through the 3D volume of the next available snapshot (Figure 16). We keep moving along the same LOS in 3-D space, but we have just shifted to a new instant in the time records of the hydrocode. The above temporal shift is repeated as many times as required by the relevant criterion along the LOS, until the spatial end of the LOS.

31

8.3.3. Aiming the line of sight

The direction of a LOS in 3D space is defined by the two angles of azimuth (angle 1) and elevation (angle 2) (Figure 14), where the plane of angle 1 is the x′y′ plane, parallel to xy. For a jet parallel to the y axis, the angle between the local jet matter velocity $\vec{u}$, and the LOS, losu=$(\widehat{L\vec{O}S, \vec{u}})$, is usually small, when angle 1 approaches 90 degrees, and vice versa (Figure 18). As is well known [15], the angle losu affects the relativistic emission calculations.

Short of jet precession occuring, the plane of angle 2 (elevation) is largely perpendicular to the jet when angle 1 is zero, while it is roughly parallel to the jet when angle 1 is 90 degrees. Usually, the jet bears an approximate cylindrical symmetry, meaning that for a small angle 1, by varying angle 2, we 'rotate' the view around the jet axis, producing similar intensities throughout the way. In summary, for a jet moving along the y axis, the smaller angle 1 is, the less difference varying angle 2 makes.

On the other hand, for angle 1 nearing $\pi/2$, varying angle 2 rotates the view within a plane approximately parallel to the jet, resulting to considerable differences. Consequently, the larger angle 1 is, the stronger the effect, on the synthetic image, from changing angle 2.

8.4. Frequency-shift

This area only refers to EM waves, not neutrinos.

Radiation emitted at a given frequency, from fast-moving jet matter, is taken to be Doppler shifted in frequency

$$f_{obs} = f_{calc}D \qquad (48)$$

where f_{obs} is the observed frequency and f_{calc} is the frequency used in the emission calculations, performed in the jet frame of reference [15]. In order to accomodate for the shift, a power-law spectrum, falling off with frequency, is employed

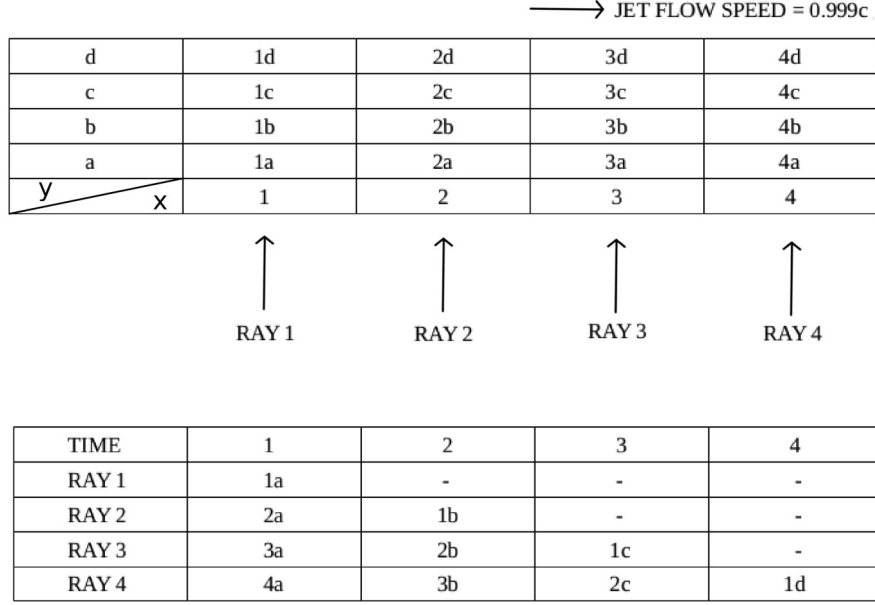$$S_{obs(f)} \propto f^{-\alpha} \qquad (49)$$

32

→ JET FLOW SPEED = 0.999c

d	1d	2d	3d	4d
c	1c	2c	3c	4c
b	1b	2b	3b	4b
a	1a	2a	3a	4a
y　　x	1	2	3	4

RAY 1　　RAY 2　　RAY 3　　RAY 4

TIME	1	2	3	4
RAY 1	1a	-	-	-
RAY 2	2a	1b	-	-
RAY 3	3a	2b	1c	-
RAY 4	4a	3b	2c	1d

Figure 17: Simultaneous advance, in both space (2D) and time, of a few lines of sight. Top half depicts the spatial situation at t=1. Sixteen jet matter portions currently occupy this mini 4 by 4 grid. Each piece of matter is named after its position at t=1 and retains that name as it moves along. The bottom half shows how the situation evolves as time marches on, with light rays meeting different jet segments that cross their path. A dash means a light ray meeting jet matter other than the above, or nothing at all.

with α assumed, as an approximation, to take the value of $\alpha = 2.0$, generally referring to the optically thin region of the jet. For D $\geq$ 1, emission is calculated at a frequency lower than the observed, resulting to a higher intensity, since the spectrum employed generally decreases with frequency.

Alternative frequency shift. RLOS may include different emission dependencies on frequency, where we calculate intensity at f_{calc} and observe that at f_{obs}.

At the moment, the above is included only as a quantitative indicator, where intensity may be optionally multiplied by the square of the ratio $f_{calc}/f_{obs} = 1/D^2$, partially negating the effect of Doppler boosting.
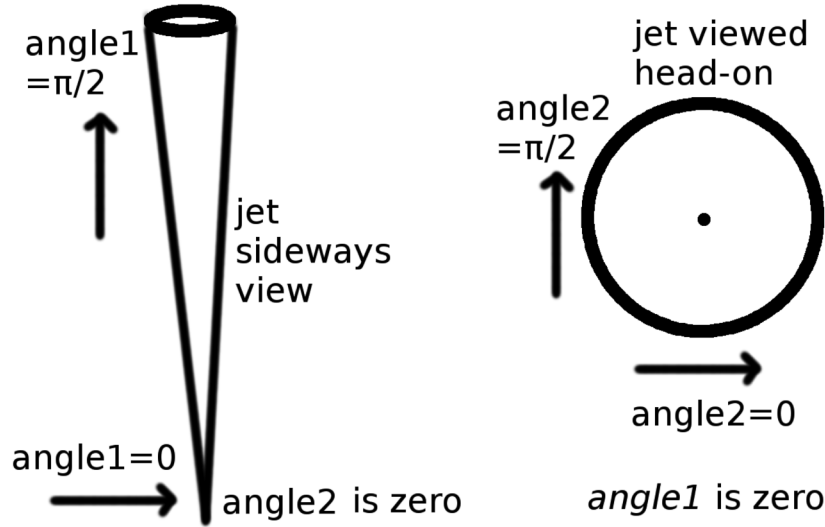
33

Figure 18: The geometric arrangement with regard to the viewing angles in the model, for the special cases of angle2 = 0 (left) and angle1 = 0 (right). For each sub-case, the arrow shows the direction of the LOS, which is different than the reader's direction of view.

9. RLOS210

⁴⁵⁰ RLOS version 2.10 was ready in November 2019. It includes a unified, functionalized, modular approach. Both XZ and YZ versions have now been unified, for both focused beam amd also parallel LOS's. Code was re-organized and a series of tests are included.

0

⁴⁵⁵ *9.1. RLOS210 commentary transcript*

This is the latest version of rlos. Version 2 is a major upgrade of the original rlos code. This time the program is broken up into procedures and functions, with a modular structure.

The program allows the user to select which case to simulate, through an ⁴⁶⁰ external parameter file. There is a unified approach, where the same modules operate on different geometries, through parameterization.

The user may select the values of the parameters of rlos version 1, and fully employ them. As menitoned above, there is no more a different version of rlos for XZ and YZ plane image formation. Now, there is one version of the code for both cases. Furthermore, for each of those cases the user may select either radiograph or camera obscura imaging tachnique.

Radiograph has all Lines of Sight parallel to each other, just like rlos v.1. This means the film (fiducial imaging screen) is the size of the scene (grid), like an X-ray medical image. The latter type of image shows clearly the various details of the system.

On the other hand, camera obscura, or focused beam, has a focal point, where the eye of the fiducial observer is located. The imaging screen, in camera obscura, is also of varied size: It may be equal, or smaller to the grid slice, at a given point along either x or y axis, depending on YZ or XZ imaging plane case. At the moment, the fiducial imaging screen must be parallel to the corresponding side of the grid, i.e. either XZ or YZ. Screen location on-axis may vary within the grid. The smaller the screen, the smaller the image.

The focal point may reside either on the side of the grid, or outside the grid, but within the limits of the projection of the XZ or YZ plane. It may have negative or zero axis position, but its two planar coords must be smaller than the grid size.

Direction angles are no longer necessarily constant throughout the calculation: for the focused beam case, each LOS is drawn with a different set of azimuth (phi1) and elevation (phi2) angles. Angles are calculated using the lines that connect the focal point and the imaging screen point, which is the target point for the LOS.

The LOS then begins from the focal point, if it resides on the grid side, or from the LOS entry point, calced suitably (here recent relevant calc, upgrade of bversion 2.10). From then on, it advances using aiming algos, trying to pass through the targeted screen point. It normally gets the target, or misses it closely! In general, the higher the resolution, the better the accuracy in this respect.

For GR pseudo-Newtonian simulations, a logical next step is to introduce D(phi1), D(phi2), i.e. alter angles along a LOS, from cell to cell, according to the effect of the potential.

Then, jet production may be imaged, if the hydrocode can employ external forces from a Kerr BHole.

9.1.1. Back in time integration along the LOS

In this version, calculations may be done either ahead in time, or backwards in time, from a selected time instant (tpicked) backwards. For camera obscura, back in time is generally the correct way to proceed. For radiograph, ahead in time also works fine, assuming a suitable fiducial setup of the jet system vs the observer. tpicked is only employed when back in time switch is activated in the external param file. tpicked must be generally towards the end of the pre-selected range of dump files, or timeshots, to be loaded to RAM. Suffcient backwards time range must be provided, for the LOS to travel back through time without reaching the beginning of the gris. Else, code cannot finish integration along LOS. When testing, the facility of altering light speed, from rlos1, may be used to play and study this effect.

Pathfinding algos have been upgraded for this version. For each combination of XZ or YZ and radiograph or camera obscura, a certain set of such pathfinders are employed.
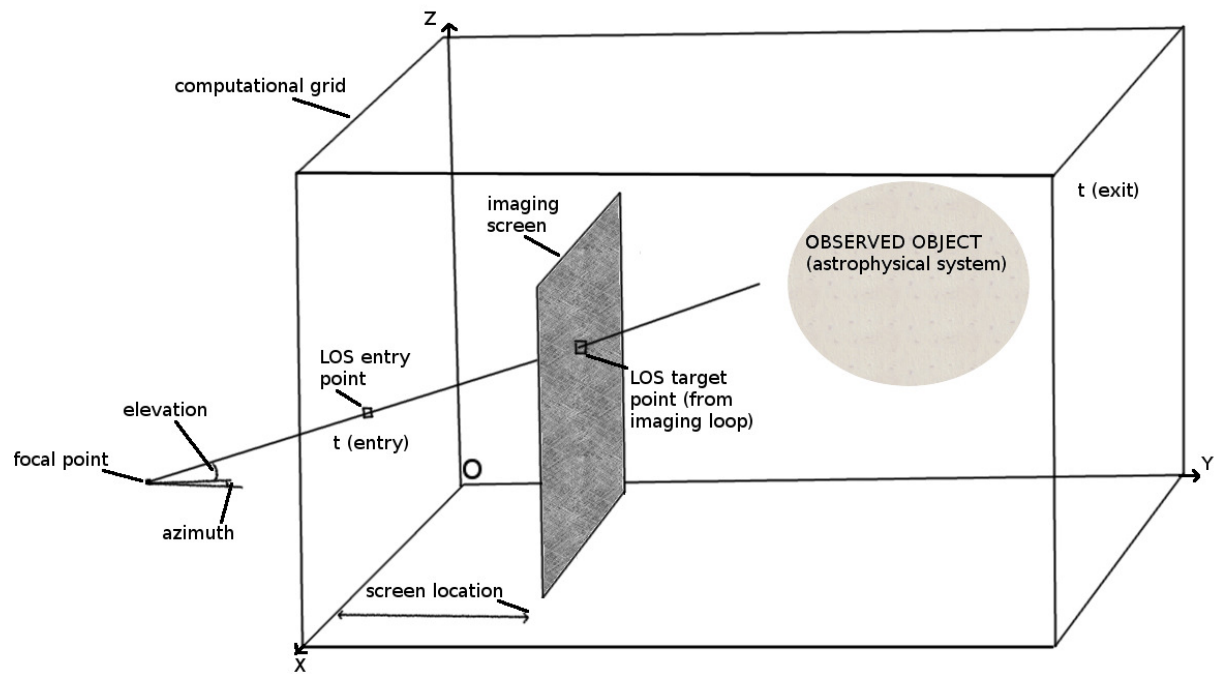
9.2. Flow diagrams

36

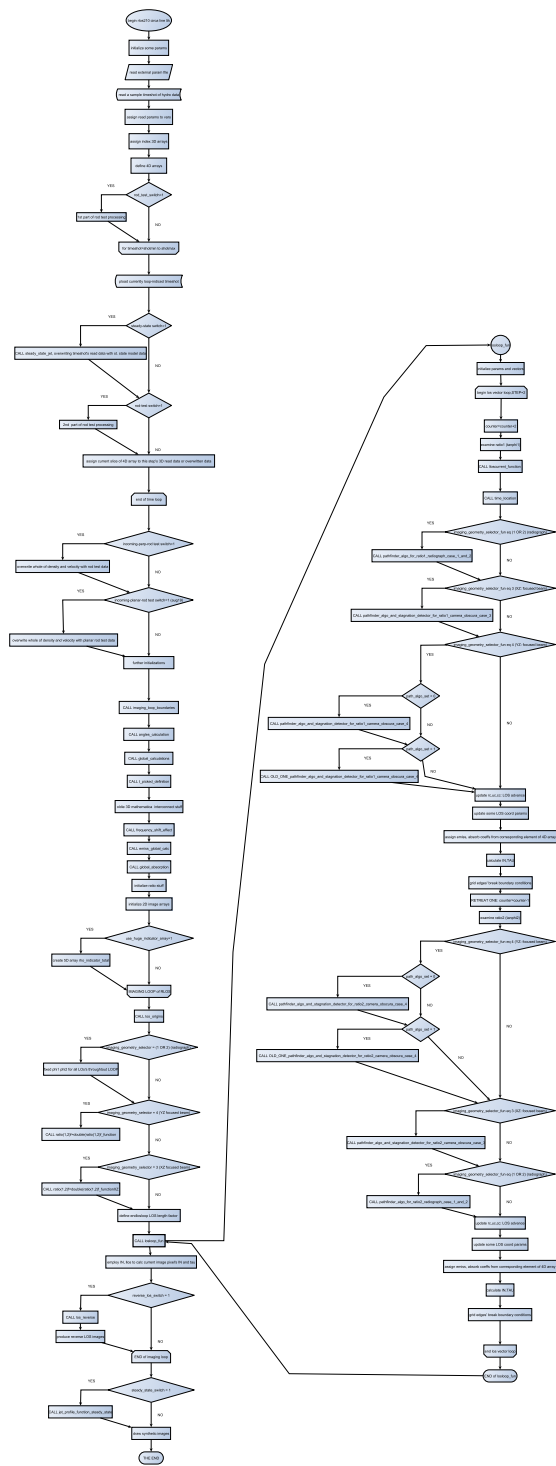Figure 19: The geometry of focused beam imaging in rlos.

Figure 20: A flow diagram of rlos2.1, depicting the procedures and functions called during program execution. A separate sub-diagram is provided for the main subroutine that draws the LOS.
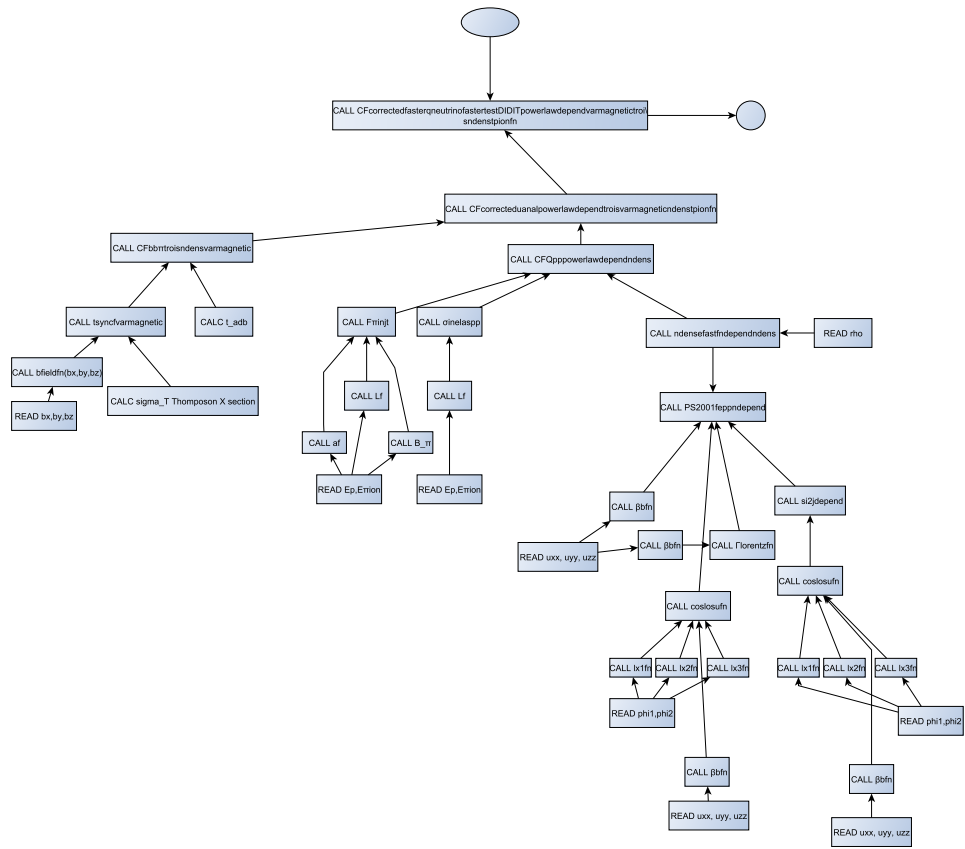
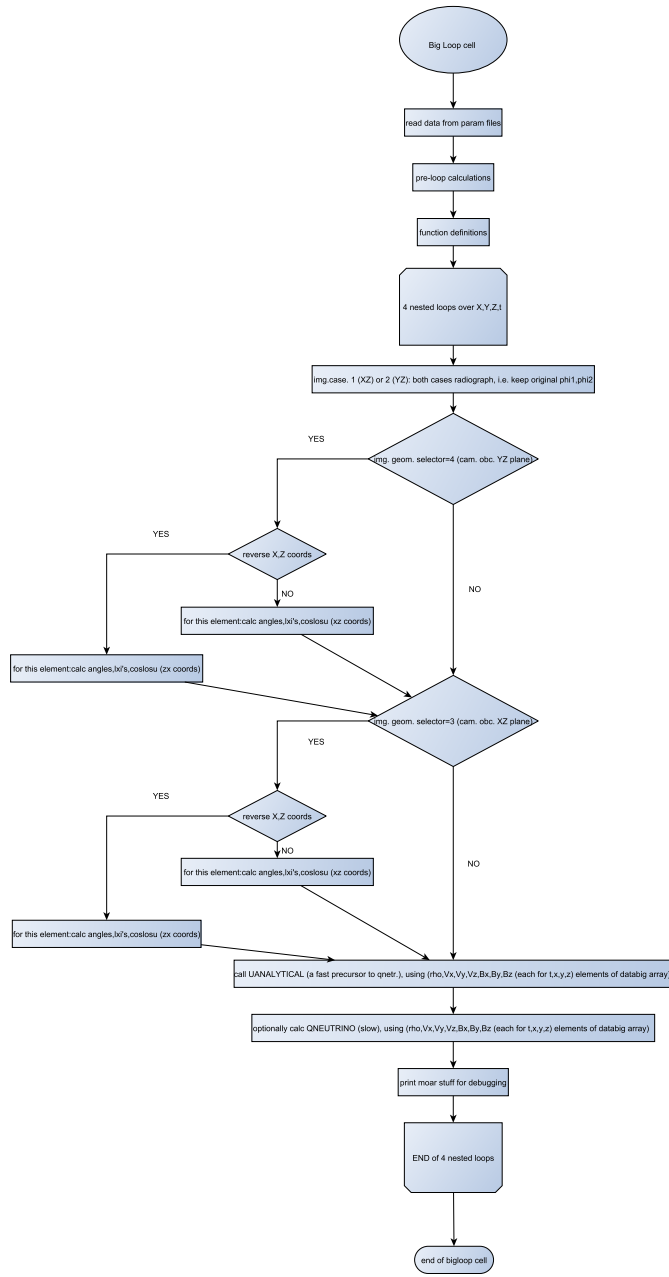Figure 21: A flow diagram of nemiss, depicting the basic structure of the program.

Figure 22: A flow diagram of the main loop of nemiss, where the calculation takes place. This has now been upgraded to 5D, with the addition of a loop for particle energy.